Monsoon Gyres of the Northwest Pacific: Influences of ENSO, the MJO, and the Pacific–Japan Pattern

JOHN MOLINARI AND DAVID VOLLARO

Department of Atmospheric and Environmental Sciences, University at Albany, State University of New York, Albany, New York

(Manuscript received 18 May 2016, in final form 22 November 2016)

ABSTRACT

An objective definition of monsoon gyres in the northwest Pacific was developed in order to construct a gyre climatology. Over a 31-yr period, 53 gyres were identified with a median formation location at 16.5°N, 135°E. More than 80% formed during July–September. More than half of gyres developed during El Niño periods at a median location 1200 km farther to the east-southeast than during La Niña. Cyclonic winds at 850 hPa extended across a diameter of more than 4000 km, with maximum tangential wind near the 1000-km radius. A precipitation maximum extended westward for several thousand kilometers south of the gyre. Typhoons were most common north and east of the gyre centers. More than 70% of gyres developed during large-amplitude MJO events, with a strong preference for Real-time Multivariate MJO (RMM) phases 5–7. In boreal summer these phases contain circulation and convective anomalies that coincide most closely with those of the climatological monsoon trough. Gyres are most likely to form when an active, large-amplitude MJO event superposes with the monsoon trough in the presence of high sea surface temperature. Gyres exhibited 850-hPa wind, height, and vorticity anomalies and surface latent heat flux anomalies that closely resembled the active Pacific–Japan pattern (PJP). This was especially true during La Niña, even though no attempt was made to isolate the PJP. It is hypothesized that an active MJO modulates gyre formation, and the gyres project onto the active phase of the PJP as they move westward.

1. Introduction

Lander (1994) first identified monsoon gyres in the northwest Pacific as a separate class of disturbance in a case study from 1991. Their primary characteristics were the exceptionally large diameter of the closed surface pressure contour, long lifetime, and relatively rare occurrence. Winds were typically light at the gyre center, and strongly asymmetric clouds and precipitation peaked south and east of the center.

One consequence of the size of the gyre is that tropical cyclones tend to form to the east or southeast and rotate around the gyre center. An example of this behavior was displayed by Crandall et al. (2014, their Fig. 1): a tropical cyclone formed to the south, moved cyclonically three-quarters of the way around the gyre, and then abruptly turned northwestward. Carr and Elsberry (1995), Wu et al. (2011), and Bi et al. (2015) argued that such track shifts resulted from nonlinear interactions between the gyre and the tropical cyclone. Crandall et al. (2014) noted that a tropical cyclone circling a gyre was mislocated in real time by 465 km, and was assigned two different names when postseason processing showed only one storm was present.

Surface westerlies and southwesterlies often exceed gale force southeast of gyre centers. These gales greatly complicate shipping forecasts by the Joint Typhoon Warning Center (JTWC), particularly with regard to whether or not the gyres should be identified as tropical cyclones (Lander 1994). Given these many operational complications produced by gyres, a need exists to understand their formation and evolution.

Holland (1995) and Molinari et al. (2007) studied the same 1991 gyre as in Lander's (1994) paper. They found that gyre formation was preceded by frequent midlatitude wave breaking. Molinari et al. (2007) argued that the gyre represented the first low in an equatorial Rossby wave packet that lasted for 3 months. The gyre developed during an active El Niño period.

Molinari and Vollaro (2012) described three additional gyres that formed during La Niña, well to the

Corresponding author e-mail: John Molinari, jmolinari@albany.edu

DOI: 10.1175/JCLI-D-16-0393.1

north and west of the 1991 gyre. The gyres developed near the leading edge of the MJO. Breaking waves induced by MJO convection to the west appeared to play a key role in gyre formation.

A complex mix of tropical disturbances exists in the northwest Pacific. Hurley and Boos (2015) examined one such disturbance, the monsoon depression. These disturbances are smaller in scale than monsoon gyres, with a typical radius of maximum winds of about 300 km. Hurley and Boos (2015) found that monsoon depressions were more frequent over land than over water. They did not contain tropical cyclones in their periphery. These characteristics make monsoon depressions separable from larger-scale monsoon gyres. The criteria for gyres used in this paper will include a diameter of cyclonic winds that exceeds 4000 km, and the vast majority of times will contain tropical cyclones within 1000 km of the center. It will be argued, similar to Lander (1994), that monsoon gyres represent a distinct type of disturbance.

The previously described monsoon gyre papers examined individual case studies. Wu et al. (2013) constructed a gyre climatology for the northwest Pacific. They found maximum tangential wind at 850 hPa between 800 and 1100 km radii [see Fig. 6 in Wu et al. (2013)]. The disturbances were warm-core from 850 to 300 hPa. Gyre frequency peaked in August and September. Nearly 20% of northwest Pacific tropical cyclones in their climatology formed in the vicinity of monsoon gyres. The goal of the current paper is to extend the work of Wu et al. (2013) by developing an objective gyre definition and by exploring the roles of ENSO, the MJO, and the Pacific–Japan teleconnection pattern (PJP) in gyre formation and evolution.

2. Data and methods

a. Data sources

Twice-daily ERA-Interim (ERA-I) analyses (Dee et al. 2011) provided wind, height, and temperature at 39 vertical levels with 1.5° latitude–longitude resolution. ERA-I analyses of sea surface temperature (SST) and surface sensible and latent heat fluxes were also incorporated. The surface fluxes in the analyses are ''accumulated'' variables that represent an average over a 6-h integration of the model. This was deemed acceptable because surface fluxes vary fairly slowly in time, and no reliable alternative source exists.

Daily rainfall data were obtained from the PERSIANN dataset (Ashouri et al. 2015). This is based on hourly data summed over 24-h periods centered at 1200 UTC. Precipitation could have been obtained from ERA-I in the same manner as the surface fluxes, but given the more rapid variation of precipitation in the model, the observed PERSIANN values were considered superior.

Composite streamfunction ψ and velocity potential χ will be displayed. Calculation of these variables over a limited area produced substantial artifacts because the Helmholtz theorem is valid only over a global region without boundaries. As a result, even though these fields will be plotted over a limited area, they were calculated over a global grid at each gyre time.

El Niño and La Niña were identified by values exceeding ±0.25°C in the Niño-3.4 anomaly,[1] averaged over June–November of each year. Smaller anomaly magnitudes were defined as ENSO-neutral. Tropical cyclone positions were obtained from the Joint Typhoon Warning Center. Real-time Multivariate MJO (RMM) values[2] (Wheeler and Hendon 2004) provided a measure of the MJO state. All data covered the 31-yr period from 1983 to 2013. Anomalies of all fields represent the deviation from the daily 31-yr mean at each point with respect to the gyre center. Only June through November were considered for this analysis.

b. Gyre definition

Previous papers on gyres used subjective, nonquantitative definitions of gyre existence and center position (see the appendix for details). Gyres seem unmistakable when viewed with satellite images overlaid on lower-tropospheric wind fields [see, e.g., Figs. 2 and 16a,b from Molinari and Vollaro (2012)]. One goal of this paper was to produce quantitative, reproducible definitions that are compatible with this subjective recognition of gyres.

The four criteria for the presence of gyres are listed in Table 1. First, 850-hPa circulation (and thus azimuthally averaged tangential velocity) had to be cyclonic at every radius from 100 to 2000 km. This insured the presence of the huge cyclonic circulations described by Lander (1994) and by the three case studies of Molinari et al. (2007), Molinari and Vollaro (2012), and Crandall et al. (2014). Second, 850-hPa circulation averaged over 900–1200-km radii exceeded a critical value $C_{\min}$. This criterion removed broad but weak cyclonic circulations such as the monsoon trough. It also removed ordinary tropical cyclones, whose circulation approaches zero at those radii. The appendix provides more details, including how the value of $C_{\min}$ was chosen.

The third criterion set the minimum time period to 4 days. This avoided the counting of transient interactions

[1] See http://www.ncdc.noaa.gov/cdr/operationalcdrs.html.
[2] See http://www.esrl.noaa.gov/psd/mjo/mjoindex/.

TABLE 1. Criteria for identification of monsoon gyres; $C = rv_\lambda$ refers to azimuthally averaged circulation at 850 hPa.

Criterion	Purpose
$C > 0$ for each 100-km radial bin for r = 100–2000 km	Insures large cyclonic circulation
$C > C_{min}$ averaged for r = 900–1200 km.	Removes broad weak circulations like the monsoon trough; removes ordinary tropical cyclones; C_{min} chosen based on three previously studied gyres
Time period satisfying the above two conditions ≥4 days	Removes transient gyres created, for instance, when horizontal shear brings two tropical cyclones toward one another, then apart
Any existing typhoon within r = 1000 km rotates around the gyre	Removes exceptionally large tropical cyclones that otherwise satisfy the top three criteria; removes gyre times when a typhoon and the gyre cannot be separated

that produced a short-lived gyre, such as two tropical cyclones brought together and then apart by horizontal shear. The fourth criterion was required to satisfy two remaining problems: 1) unusually large tropical cyclones fit the gyre criteria but failed to display the dramatic asymmetries and larger-scale structure of gyres described in previous work; and 2) tropical cyclones sometimes formed near the center of existing gyres (e.g., Lander 1994). If the tropical cyclone shifted too close to the gyre center, vorticity interactions made them impossible to distinguish from the gyre. This is reflected in the idealized experiments by Liang and Wu (2015): when an idealized tropical cyclone was placed 400 km from an idealized gyre, it did not rotate around the gyre, and the two could not be separated.

Both of these issues were eliminated by the fourth criterion: the tropical cyclone had to rotate cyclonically with time around the gyre center. If it did not, the gyre was not separable from the tropical cyclone, and was not counted. This criterion also removed the previously noted large tropical cyclones, which moved together with the defined gyre center rather than around it. Additional discussion of the methodology is provided in the appendix.

The above criteria produced 53 gyres during June–November between 1983 and 2013, 1.7 per year. This number fell between the estimates of Wu et al. (2013) of 3.7 per year during the warm season, and Lander (1994), who estimated one gyre every two years. Most of the gyres (81%) formed between 1 July and 30 September.

3. Influences of ENSO and the MJO

The tracks of gyres are given in Fig. 1 for three ENSO phases: El Niño, La Niña, and ENSO-neutral. The mean ITCZ/monsoon trough structure for each phase is given by the shaded 850-hPa relative vorticity field, following the definition of Molinari and Vollaro (2013). The phrases "initial time" or "formation time" define the first time the gyres met the four criteria in Table 1, but preexisting weaker disturbances preceded that time. Gyres were more likely to form during El Niño (53%) than La Niña (28%). Every El Niño gyre first met the criteria equatorward of 22°N, with 86% forming within the mean monsoon trough. Both the median gyre formation point and median overall center position for El Niño gyres were located about 1200 km southeast of those for La Niña.

All but two La Niña gyres formed poleward of 15°N, and all but one west of 140°E. Nearly half formed poleward of the mean monsoon trough, suggestive of midlatitude influences (Molinari and Vollaro 2013). The locations of the 10 ENSO-neutral gyre formations fell almost halfway between those of the other ENSO phases. The median formation location for all gyres was found at 16.5°N, 135°E.

At the times of gyre formation, the mean SST within the 1000-km radius was 29.3°C during El Niño and 29.1° during La Niña. SST anomalies were negative and less than 0.2°C in both. As a result, gyres developed over warm but not anomalously warm water regardless of the ENSO state. The mean intensity for all gyre times (measured by 900–1200-km circulation; not shown) was virtually identical for the three ENSO phases.

The impacts of ENSO on tropical cyclone genesis and evolution have been well documented (e.g., Chan 1985; Chia and Ropelewski 2002). Similar to tropical cyclones, gyre formation shifts southeastward and exhibits longer tracks during El Niño (Camargo and Sobel 2005). Unlike for tropical cyclones, overall gyre frequency increases and mean gyre intensity remains unchanged during El Niño.

The influence of the Madden–Julian oscillation on gyres was as dramatic as that of ENSO: 73% of all gyre times (and 74% at formation) occurred during RMM phases 5 to 7 (Fig. 2). Gyres were less likely to occur in phases 4 and 8, and were rare in phases 1–3. The majority of gyres (70%) were accompanied by RMM amplitude exceeding unity. The gyre distribution by RMM phase was very similar for El Niño and La Niña (not shown). This reflects the effective removal of long time scale phenomena from the RMM definition (Wheeler and Hendon 2004).

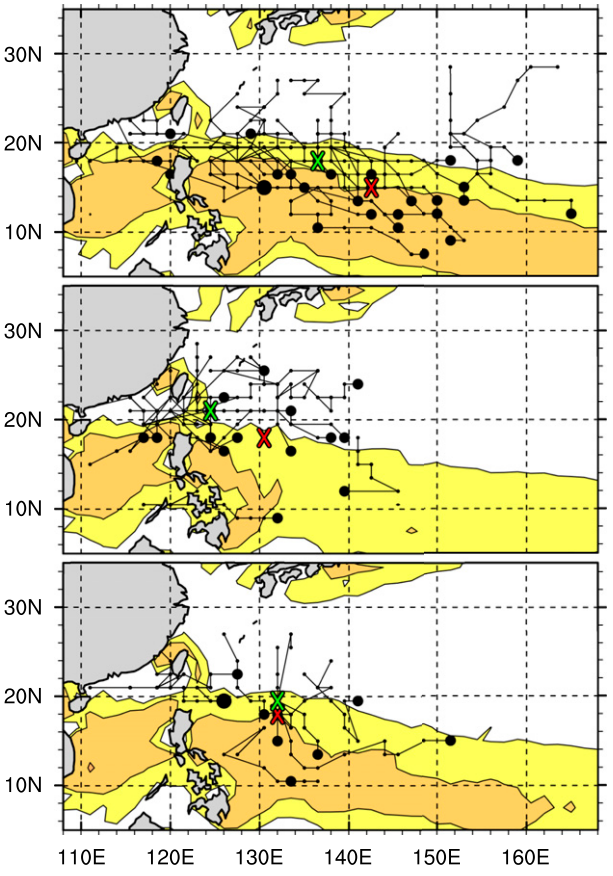

FIG. 1. Gyre tracks during (top) El Niño, (middle) La Niña, and (bottom) ENSO-neutral periods. The filled black circles indicate the beginning of the track; a large circle indicates that two gyres formed at the given point. The red and green X's represent the median gyre formation location and median overall location, respectively, during each ENSO phase. The shading shows 31-yr mean June–November vorticity during each phase. Yellow: 0–4 × 10^{-6} s^{-1}; orange: >4 × 10^{-6} s^{-1}. ENSO states are delineated using June–November Niño-3.4 anomalies exceeding ±0.25°C.

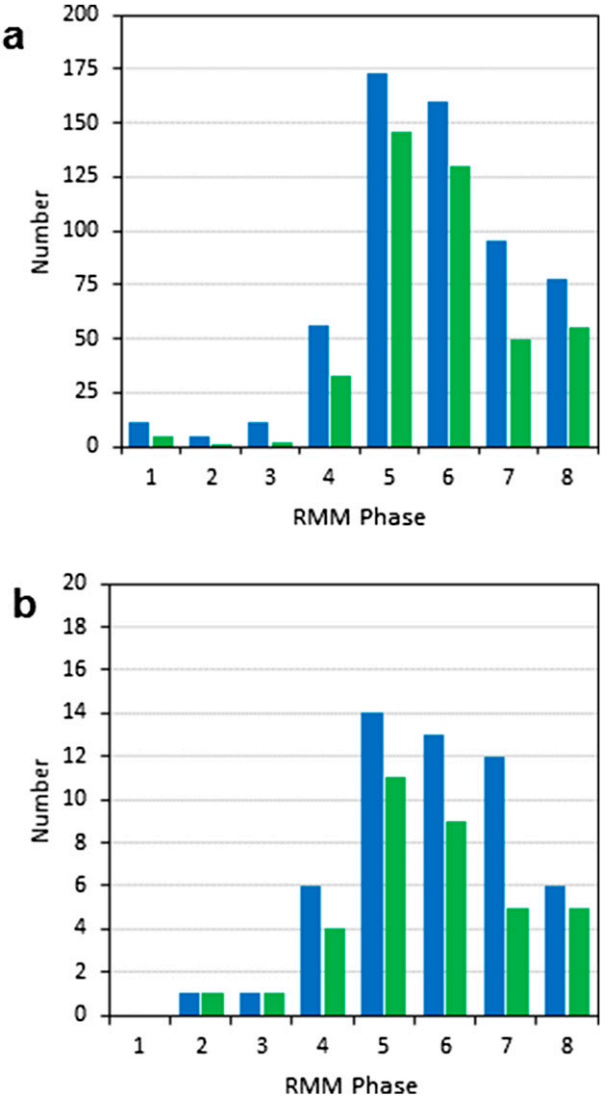

FIG. 2. (a) Distribution of all gyres vs the MJO phase defined using the RMM index (Wheeler and Hendon 2004). Blue bars: total number of gyres for each phase. Green bars: number when the RMM amplitude exceeded unity. (b) As in (a), but for only the initial gyre time periods.

The MJO influences on gyre location and frequency were comparable to those for tropical cyclones (Liebmann et al. 1994; Nakazawa 1988). Tropical cyclone frequency peaks in phases 5–7 and is small in phases 1–3 (Camargo et al. 2007, 2009). Overall, gyre distribution and track, but not intensity, have similar variations with respect to the ENSO and MJO states as tropical cyclones.

4. Gyre characteristics

Gyres appear to have a major influence on the location of strong tropical cyclones with respect to the gyre center (Fig. 3). Most of the 36 typhoon-strength disturbances were found within 1000 km of the gyre centers, predominantly to the north and east. Similar to the studies by Lander (1994), Molinari et al. (2007), and Crandall et al. (2014), tropical cyclones tended to intensify east of the gyre, move around it, then weaken below typhoon strength or "escape" to the north and northwest. The pronounced asymmetry in storm location suggests that gyres might initiate as equatorial Rossby waves (Frank and Roundy 2006; Molinari et al. 2007).

An additional 45 tropical storms and depressions were present within 1000 km, but are not shown because the gyre itself is sometimes labeled a depression (and rarely, a storm) by JTWC. Overall, 81 tropical cyclones existed within 1000 km of 53 gyres, about 1.5 per gyre. This is roughly equivalent to Wu et al. (2013), who found

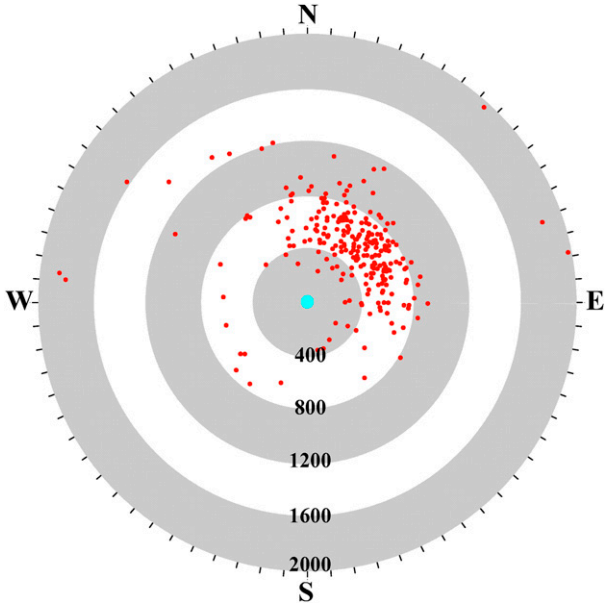

FIG. 3. Twice-daily locations with respect to gyre centers of all typhoons occurring within 2000 km of a gyre for the period between 1983 and 2013.

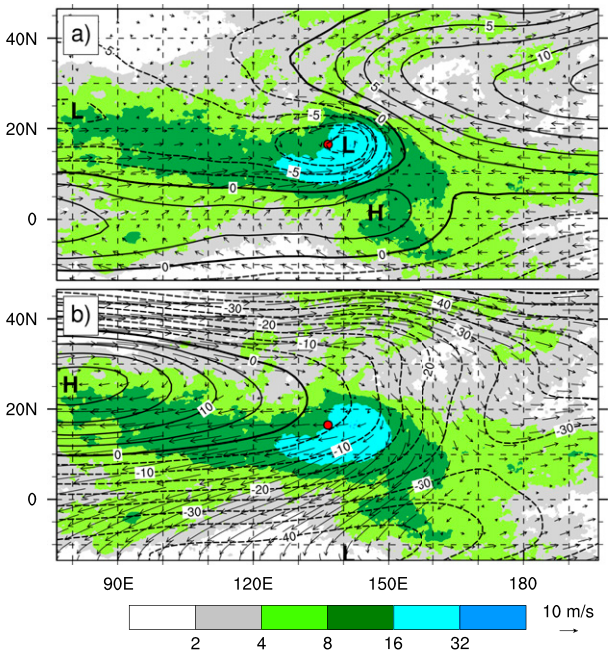

FIG. 4. (a) Composite total 850-hPa horizontal wind (vectors) and streamfunction ($10^6\,m^2\,s^{-1}$; black contours) at the gyre initial times. Also shown is the composite precipitation (mm day^{-1}). The gyre center is given by the filled red circle. (b) As in (a), but for 150 hPa. Latitude and longitude are defined with respect to the composite gyre center. Wind vectors with magnitude less than 1 m s^{-1} are not plotted.

1.1 tropical cyclones per gyre. Over the 31 years of this study, 775 tropical cyclones (443 of which reached typhoon strength) developed in the northwest Pacific. Gyres thus were associated with about 10% of tropical cyclones. This percentage is half that of Wu et al. (2013), consistent with their definition producing about twice as many gyres. Tropical cyclones often remained in the gyre vicinity for one or more days. As a result, 87% of 12-hourly periods in gyres in this study contained a tropical cyclone within 1000 km of the center.

On average the gyres moved toward the northwest at 2.5 m s^{-1}. The median gyre lifetime of 5 days fell short of mean times of 8 days found by Wu et al. (2013) and up to two weeks by Lander (1994). The definition in this paper included only those times the gyre circulation exceeded the C_{min} criterion. Large circulations not meeting the criterion often existed before and after; the mean lifetime would be longer if the gyres were tracked until they disappeared. The longest duration gyre existed from 11–22 August 1991.

This section will display the horizontal structure of gyres only at their initial times, combining all the ENSO states. Maximum tangential velocity (not shown) existed near the 850-hPa level and 900–1000-km radii, nearly identical to the mean structure identified by Wu et al. (2013). Cyclonic flow extended about 1000 km farther from the center compared to a strong tropical cyclone (see Fig. A1d in the appendix).

Composite total 850-hPa wind and streamfunction in addition to precipitation at the initial gyre times are shown in Fig. 4a. The composite gyre center is indicated by the filled red circle. Three large-scale features existed in the streamfunction field. The monsoon trough extended west-northwestward at 10°–20°N from the longitude of the gyre to the Bay of Bengal. Precipitation peaked within and equatorward of the monsoon trough. Northeast of the gyre, the broad anticyclonic flow of the subtropical high exhibited a precipitation minimum. The equatorial ridge existed where air was crossing the equator from the south. It might represent the influence of opposite-signed absolute vorticity carried by cross-equatorial flow from the Southern Hemisphere.

The gyre for this initial time composite was located at the eastern end of the monsoon trough, a region where disturbances often intensify (Ritchie and Holland 1999) in the presence of background convergence (Sobel and Bretherton 1999; Molinari et al. 2007). Westerlies and easterlies converged at the gyre longitude, qualitatively similar to the off-equatorial Gill (1980) response to diabatic heating. Within the gyre, the center of circulation and the precipitation maximum were shifted slightly east of the center. Wind speed was light near the center, consistent with Lander (1994).

Wu et al. (2013) and Chen et al. (2004) included the presence of asymmetric precipitation as a part of the

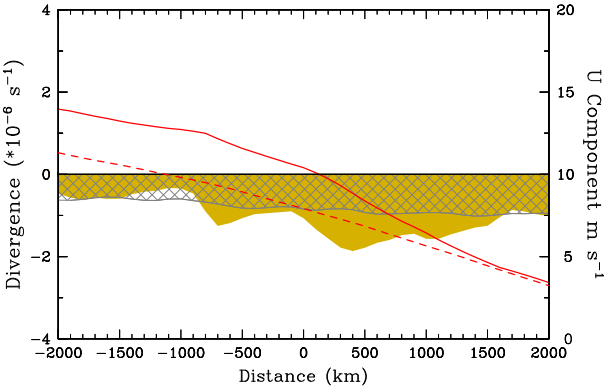

FIG. 5. The 850-hPa total zonal wind (m s^{-1}; solid red line) and climatological zonal wind (red dashed line) for gyres at their initial time over a 2000-km latitudinal region centered on the gyre. Light brown shading: total zonal divergence; cross-hatched: climatological zonal divergence; both $\times 10^{-6}$ s^{-1}.

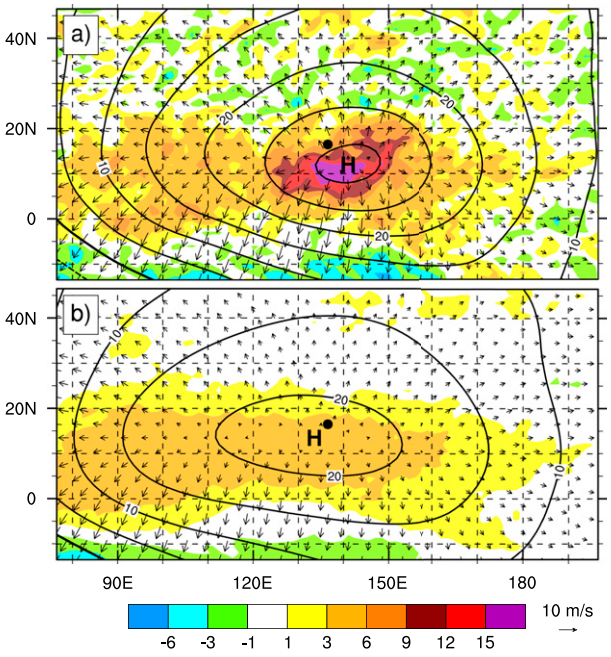

FIG. 6. Composite 150-hPa velocity potential (χ; contoured), divergent wind vectors, and horizontal divergence (10^{-6} s^{-1}; shaded) at the initial times of gyres: (a) total field and (b) climatological mean. Divergent wind vectors less than 1 m s^{-1} are not plotted. The black dot represents the composite gyre center.

gyre definition. Although precipitation structure was not considered as part of gyre identification in this paper, Fig. 4 shows a similar asymmetry to the two papers above. This suggests the gyre definition procedures in Table 1 and the appendix were successful in isolating disturbances with the classic structure defined by Lander (1994) and by other gyre studies.

The exceptional nature of the gyre can be seen by contrasting the precipitation asymmetry to that expected from the vertical wind shear direction. Mean vertical shear averaged over 1000 km of radius [calculated following Corbosiero and Molinari (2002)] at these initial gyre times was from the east-northeast (72°) at 6.5 m s^{-1}. A cylinder of cyclonic vorticity with that shear would be expected to have maximum precipitation downshear left, thus southwest of the center (e.g., Corbosiero and Molinari 2002; Hurley and Boos 2015). The observed precipitation showed such a maximum, but the remainder of the precipitation maximum was found upshear. This likely reflects the preference for tropical cyclones east of the center region (Fig. 3). In that sense the gyre does not behave like an isolated vortex, but rather a complex interaction of disturbances, including variations in background flow.

At 150 hPa (Fig. 4b), the Asian summer monsoon high (Krishnamurti 1971) was the dominant feature. It extended eastward to beyond the gyre longitude. Broad northeasterly flow equatorward of the precipitation maximum crossed into the Southern Hemisphere from 80° to 150°E. The zonal flow reversed at this level from that at 850 hPa. A westerly midlatitude jet existed well to the north.

Zonal wind and zonal divergence at 850 hPa were averaged over a 2000-km meridional region on either side of the gyre. Westerlies were present to the west of the gyre and easterlies to the east (Fig. 5). The background convergence associated with the monsoon trough (cross-hatched region in Fig. 5) acted over the entire diameter of the gyre. Adding the meridional divergence (not shown) doubled the total divergence but had almost no impact on the mean contribution. Overall, gyres produced their own low-level convergence fields, but in the far field the mean monsoon trough contributed an extended region of convergent flow.

The divergent wind at 150 hPa (Fig. 6) gives further insight into the relative contributions of mean and anomaly. The strongest divergence over the entire region from 90°E to the date line was found within the gyre (Fig. 6a). Divergent flow to the south extended into the Southern Hemisphere, whereas divergent flow to the north was weaker. This likely reflects the meridional gradient in background inertial stability. Once again the climatological monsoon trough region (Fig. 6b) contributed substantially to the divergent circulation, especially west of the gyre.

The 850-hPa streamfunction and wind shown earlier in Fig. 4a are separated into climatological and anomaly fields in Fig. 7. The anomaly field is simply the difference between the total and climatological fields and thus includes not only the gyre, but also the MJO and any other deviations from the mean state. It should be noted, however, that all phases of the MJO are represented (as

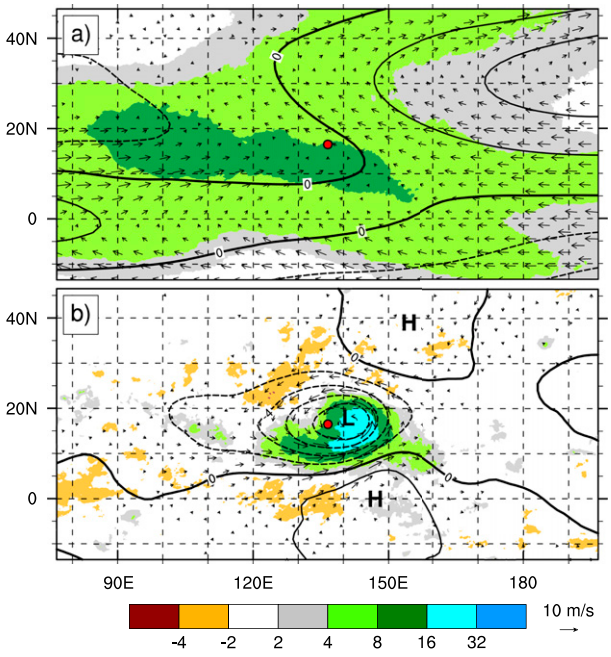

FIG. 7. As in Fig. 4a, but for (a) the 850-hPa climatological mean state and (b) the anomaly from the mean.

in Fig. 2), and thus some cancellation of anomalies will be present.

The climatological fields (Fig. 7a) show the monsoon trough and the subtropical high clearly, as well as the ITCZ extending toward the east. The anomalies (Fig. 7b) displayed a deep low and large precipitation within 1500 km of the gyre. One intriguing aspect of Fig. 7b involves the positive streamfunction anomalies south-southeast and northeast of the gyre. This pattern shares some qualities with height anomalies associated with the Pacific–Japan teleconnection pattern (PJP). This connection will be addressed in the following section.

5. Pacific–Japan pattern

The PJP has been isolated using monthly mean fields (Nitta 1987), 3-monthly mean fields (Choi et al. 2010), and 10–50-day filtered fields (Li et al. 2014). A PJP index has been defined using anomalous precipitation just east of the Philippines (from 10°–20°N and 120°–130°E) by Kosaka and Nakamura (2006), and in terms of an 850-hPa height anomaly difference between subtropical and middle latitudes by Wakabayashi and Kawamura (2004). The PJP appears to represent a convectively coupled dynamical mode that can be excited within the zonally asymmetric baroclinic mean flow in the summertime western North Pacific (Kosaka and Nakamura 2006). The active PJP is associated with anomalously large synoptic-scale variability (Li et al. 2014) and more frequent tropical cyclogenesis (Choi et al. 2010).

TABLE 2. PJP index values (m) derived from 20–100-day height anomaly differences using Eq. (1) during the times a gyre is present. Shown are values for each ENSO state, and for all gyre positions west or east of 140°E. Also given are the same height anomaly differences for two 10° longitude eastward shifts from the PJP definition. These values are for JJAS only.

	PJP index	Shifted 10° eastward	Shifted 20° eastward
La Niña	38.8	31.2	0.4
El Niño	10.8	20.5	11.5
West of 140°E	28.9	24.8	3.7
East of 140°E	−1.1	19.9	26.3

The PJP represents an intraseasonal phenomenon. To be consistent with the time scales chosen by Nitta (1987) and Kosaka and Nakamura (2006), a 20–100-day Lanczos filter was used to define the PJP index in this paper. Following Wakabayashi and Kawamura (2004),

$$\text{PJP index} = z^*_{850}(35°\text{N},155°\text{E}) - z^*_{850}(22.5°\text{N},125°\text{E}), \quad (1)$$

where z^* is the 20–100-day geopotential height anomaly. Because the PJP is strongest in boreal midsummer (Tsuyuki and Kurihara 1989), only June–September values and composite figures will be shown. However, PJP values and composite structure were similar using all months or using June through August only, owing to the small number of gyres outside midsummer.

Table 2 gives values for the PJP index for various gyre composites. In addition, the two index points are shifted eastward by 10° and 20° longitude. The first two rows of Table 2 compare the PJP index for the two ENSO states. The standard PJP index [Eq. (1)] is positive (active PJP) and much larger during La Niña than El Niño. The largest positive value during El Niño exists at 10° longitude to the east, consistent with the eastward shift in gyre locations.

A positive PJP index represents an anomalously strong low-frequency height gradient between low heights to the south and high heights to the north. Table 2 showed height anomaly differences of more than 30 m associated with the PJP for active gyre times during La Niña. The PJP anomalies are in phase with the climatological monsoon trough and subtropical high (Fig. 7a), which exhibit a 27-m difference in height between the two points. The positive PJP for gyre times during La Niña effectively doubles the background height gradient.

As seen in Fig. 1, both primary ENSO states contain gyre locations well to the west. To separate PJP values

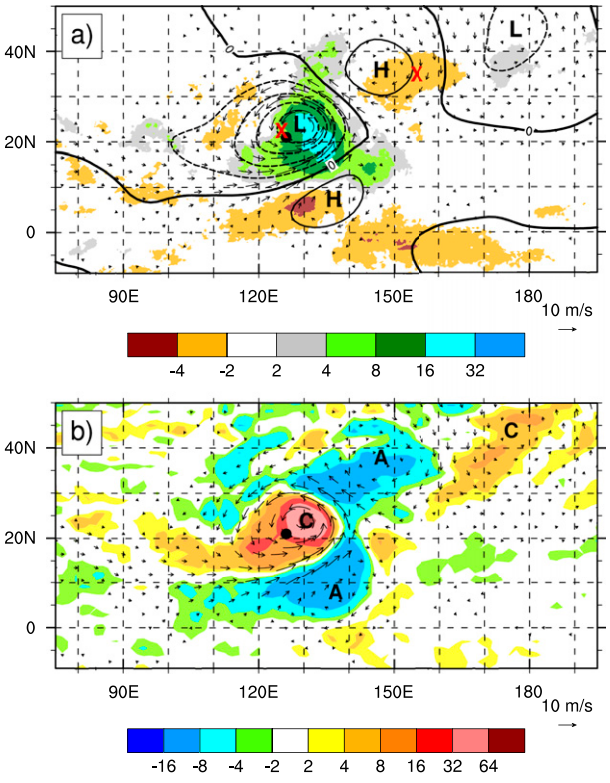

FIG. 8. The 850-hPa anomaly fields as in Fig. 7b, but for only JJAS gyres during La Niña: (a) ψ (increment $2.5 \times 10^6\,m^2\,s^{-1}$), wind, and precipitation (mm); and (b) vorticity anomalies ($10^{-6}\,s^{-1}$; shaded) and wind. In (b), C and A represent cyclonic and anticyclonic vorticity anomalies, respectively. The red X's in (a) represent the two points used for the PJP index in Eq. (1).

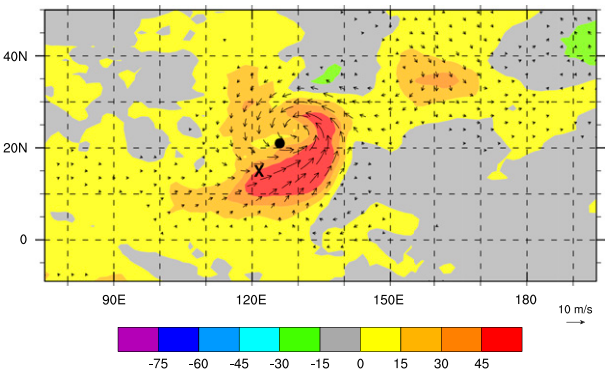

FIG. 9. Latent heat flux anomaly ($W\,m^{-2}$; shaded) for June–September gyres during La Niña. Anomalous near-surface winds are also plotted. The location of the PJP surface latent heat flux maximum (Kosaka and Nakamura 2006) is given by the black X and the composite gyre center by the filled black circle.

solely by longitude, the last two rows of Table 2 consider only gyre times east and west of 140°E, regardless of the ENSO state. Larger PJP values occur when gyres are to the west. When gyres are east of 140°E, the largest height anomalies shift 20° longitude to the east. Table 2 indicates that gyres project onto the PJP index during La Niña, and seem to project onto a PJP-like state farther east during El Niño. The latter is consistent with Kosaka and Nakamura (2006), who found that the sign of the PJP index remained the same to the east of the points in Eq. (1), but with smaller magnitude. Composite fields for La Niña closely resemble composites for western gyres; the same is true for El Niño and eastern gyre composites. As a result, only the ENSO composites will be shown.

The top panel of Fig. 8 shows 850-hPa anomaly ψ, wind, and precipitation for all gyre times during La Niña. As in Fig. 7b, this field contains all variations from climatology, including gyres and the MJO. The PJP pattern appears much more clearly than for the initial gyre times that were shown in Fig. 7b. Figure 8 shows a surprisingly similar structure to the PJP positive phase (Fig. 4a of Li et al. 2014), even though no attempt was made in this study to isolate the PJP. In particular, the positive streamfunction anomalies south of the gyre, the negative anomalies within the gyre, the positive anomalies near 40°N and 150°E, and the negative anomalies further to the east-northeast, are consistent with PJP height field anomalies shown by Li et al. (2014). Vorticity anomaly fields at 850 hPa (Fig. 8b) appear remarkably similar to those shown for the PJP by Kosaka and Nakamura (2006). The correspondence is not quite as close at 150 hPa (not shown), possibly because frequent tropical cyclones northeast of the gyres (Fig. 3) create their own local divergent circulation.

Surface latent heat flux anomalies for gyres during JJAS and La Niña in Fig. 9 are shown along with the point of maximum PJP latent heat flux (black X) from Kosaka and Nakamura (2006). The magnitude of the gyre-based anomaly at the X exceeds that of the strongest PJP events shown by Kosaka and Nakamura (2006). Based on 850-hPa wind, streamfunction, vorticity, precipitation, and surface latent heat flux anomalies, it is concluded that the gyres project remarkably well onto the PJP.

6. Discussion

a. *Composite gyre structure and distribution*

An objective definition of monsoon gyres was developed in order to create a climatology of these disturbances in the northwest Pacific. On average, 1.7 gyres formed each year, with a median lifetime of 5 days. More than 80% formed between July and September. Gyres were associated with about 10% of all west Pacific

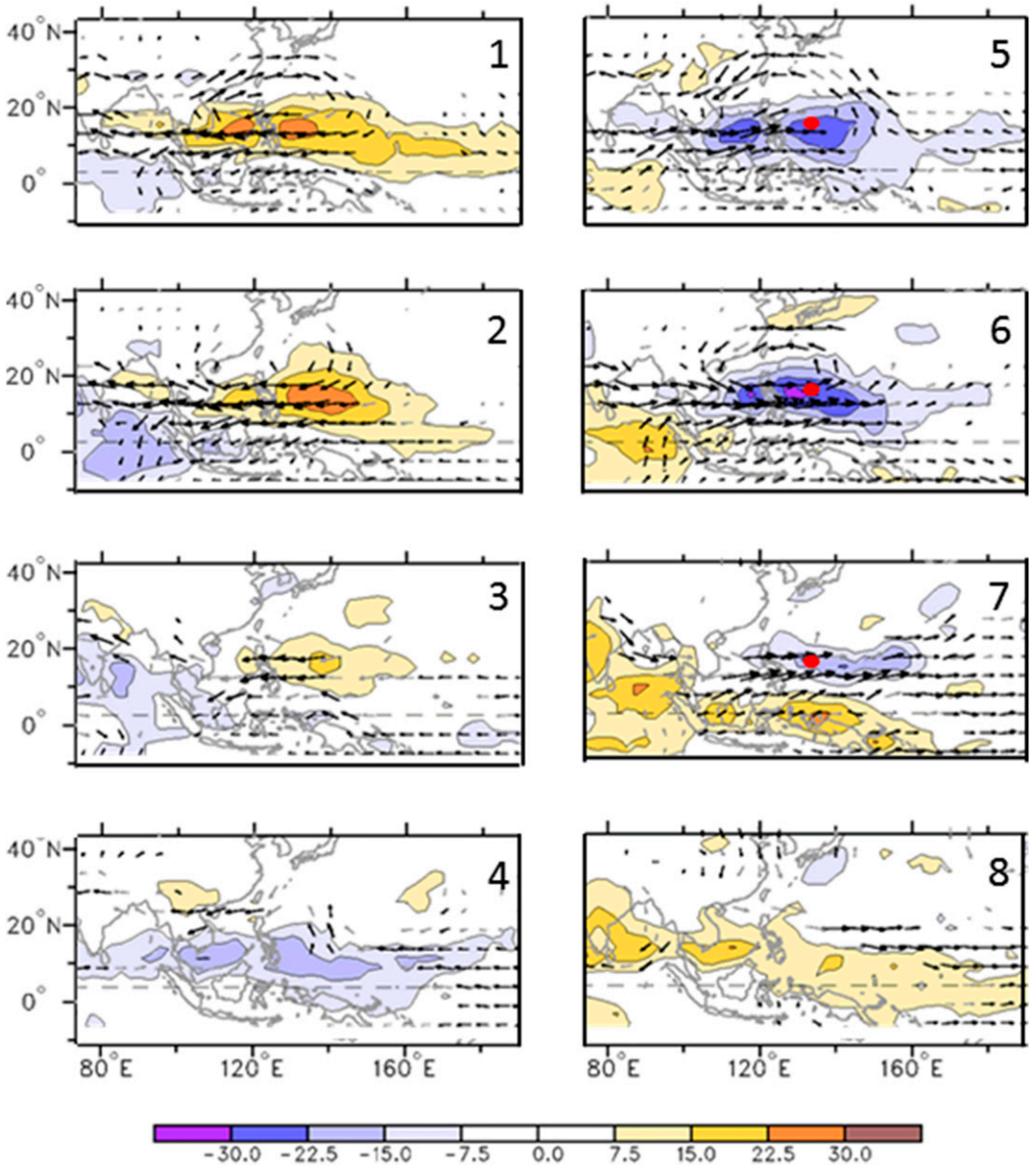

FIG. 10. Composite OLR (shaded) and 850-hPa winds (vectors) for the eight RMM states (numbers in the upper right of each panel), for July–September only. The red dot represents the median gyre formation location. This figure is based on Wheeler and Hendon (2004), and has been adapted from http://www.bom.gov.au/climate/mjo/#tabs=Average-OLR.

tropical cyclones. Their mean tangential wind and temperature anomaly structure (not shown) mirrored those of Wu et al. (2013). Gyres moved west-northwestward at an average speed of 2.5 m s^{-1}.

Gyres displayed a strongly asymmetric precipitation pattern, with maxima east and south of the center. The latter extended thousands of kilometers westward from the gyre. Gyres formed over composite SSTs above 29°C, regardless of the ENSO phase.

Monsoon gyres were strongly modulated by ENSO. More than half of all gyres formed during El Niño, with a median location 1200 km farther east-southeast compared to La Niña. Nearly all the El Niño gyres developed within the climatological monsoon trough, but La Niña gyres often formed well to the northwest, consistent with those studied by Molinari and Vollaro (2012) and Crandall et al. (2014).

The wind and precipitation asymmetries were associated with four components of the flow: the gyre itself (Fig. 7b), the MJO (Fig. 2), the PJP (Figs. 8 and 9), and frequent tropical cyclones (Fig. 3). Gyres developed within an extended region of climatological zonal

convergence associated with the monsoon trough (Figs. 1, 5, and 7a). Overall, the gyres might be viewed as complex "total field phenomena" that form and evolve in the presence of interactions among these various components.

b. What is the role of the MJO?

Figure 2 indicates an RMM amplitude greater than 1 for a significant majority of gyres. Gyre formation was most strongly favored in RMM phases 5 through 7. A composite MJO plot for JAS is provided in Fig. 10, adapted from the work of Wheeler and Hendon (2004) given at the Australian Bureau of Meteorology website.[3] The RMM composite for phases 5 through 7 reveals a large cyclonic circulation anomaly that is similar in scale to that of gyres, and a strong negative OLR anomaly south of the circulation center. The locations of these anomalies are about 5° latitude poleward of the climatological monsoon trough (Fig. 7a). In the simplest view, the formation of monsoon gyres could simply represent a strong RMM phase 5–7 vortex over sufficiently warm water that is far enough south to superpose with the monsoon trough. This sequence of events could account for the size of the gyre circulation, because the large-scale MJO interacts with the large monsoon trough. The infrequency of gyres might reflect the rarity of such a confluence of events.

Subsequent gyre behavior cannot be accounted for by the above reasoning, however, because gyres move northwestward and the MJO (more or less by definition based on its labeling in a space–time spectral plot) moves eastward. It is probable that once an MJO-influenced gyre intensifies, it couples with Earth's vorticity gradient and moves northwestward. Such a coupling would be favored by the large scale of the gyres, which creates a large difference in Coriolis parameter across the gyre. Indirect evidence for this sequence of events is provided in a Hovmöller diagram of 850-hPa meridional wind anomaly in Fig. 11. This figure examines days −10 to +4 with respect to gyre formation, composited over all gyres. A large cyclonic circulation exists near the formation point 10 days prior to the conditions in Table 1 being met. This circulation increases in intensity with time, and begins to move northwestward only near time zero, as the gyre reaches the intensity criterion in Table 1.

c. What is the role of the PJP?

One surprising result of this paper is that a clear PJP pattern arises during times that gyres are present, even though no effort was made to isolate the PJP. Anomaly magnitudes during gyre events (Figs. 8–9) are as large as those isolated using the strongest PJP events (Kosaka and Nakamura 2006; Li et al. 2014).

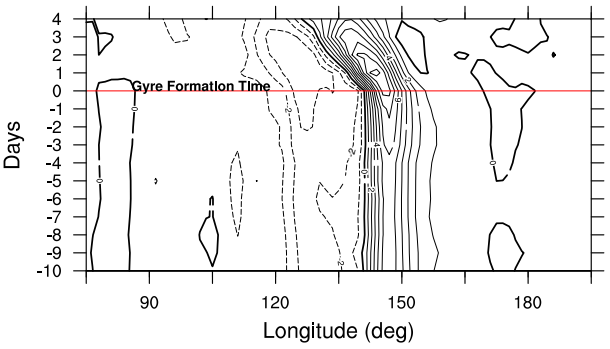

FIG. 11. Composite anomalous 850-hPa meridional wind from day −10 to day +4 with respect to the gyre formation time, averaged over all gyre formation events. This represents the mean value over a 9° latitude region centered on the composite gyre location. Contour increment 1 m s^{-1}. Dashed contours represent negative values, and the thick contour is the zero line.

We speculate on the sequence of events that gyres represent. First, gyres form most often in MJO RMM phases 5–7, when MJO diabatic heating and circulation anomalies superpose with those of the climatological monsoon trough. The gyre intensifies, moves northwestward as it interacts with Earth's vorticity gradient, and projects onto the PJP. Although gyres appear to represent distinct phenomena, they are strongly coupled to low-frequency events. The relationships among the climatological state, the MJO, the PJP, and gyre-like circulations will be the subject of future work.

Acknowledgments. ERA-Interim analyses were obtained from the National Center for Atmospheric Research, which is supported by the National Science Foundation (NSF). Dr. Ryan Torn of our department suggested using circulation as a variable for measuring gyre intensity. Sarah Ditchek generated Fig. A1d based on calculations from Ditchek et al. (2017). We appreciate thoughtful comments from Dr. Suzana Camargo and two anonymous reviewers, one of whom suggested the possible PJP–gyre connection. This paper was supported by NSF Grant AGS1249732.

APPENDIX

Details of Gyre Identification

In previous work gyres have been identified subjectively. Chen et al. (2004) required the presence of 1) a vortex more than 2500 km in diameter as estimated

[3] See http://www.bom.gov.au/climate/mjo/#tabs=Average-OLR.

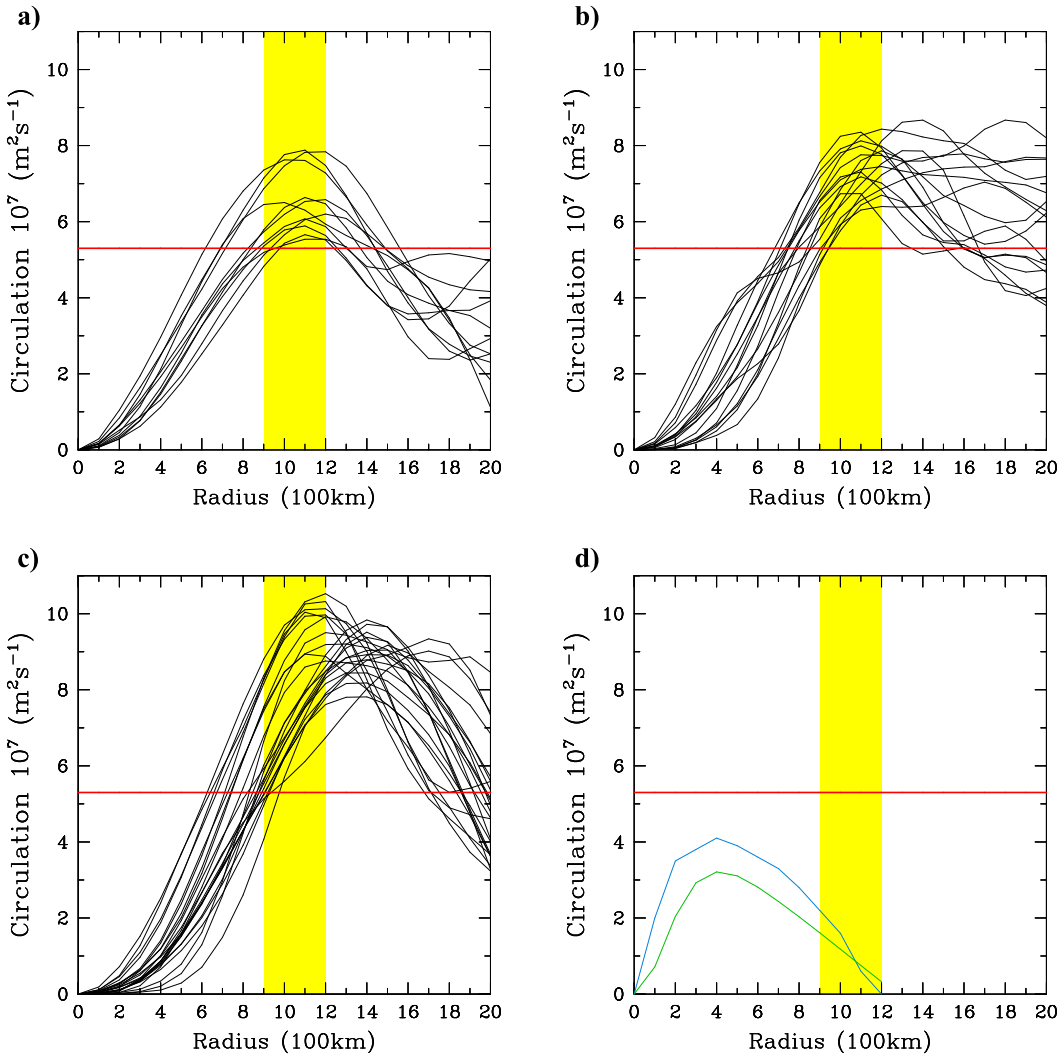

FIG. A1. Circulation vs radius for three previously studied gyres for each time the gyre met the definitions in Table 1. (a) July 1988 (Molinari and Vollaro 2012), (b) July 1989 (Crandall et al. 2014), and (c) August 1991 (Molinari et al. 2007). (d) Circulation for Hurricane Gloria (1985) (blue curve), taken from the observations of Franklin et al. (1993), and the composite circulation from 31 years of Atlantic category 3–5 hurricanes from ERA-I analyses (green curve). The blue curve is available only out to $r = 1200$ km. The green curve reaches -3×10^7 $m^2 s^{-1}$ at the 2000-km radius (not shown). The yellow bar indicates the radial range used for the C_{min} calculation.

visually from 850-hPa maps, 2) a lifetime exceeding 5 days, 3) surface anticyclones to the south-southwest and east-northeast, 4) a weak anticyclone in the upper troposphere, and 5) a sequence of small lower-tropospheric vortices to the south-southeast. Wu et al. (2013) used 10-day low-pass-filtered winds to isolate the gyre. They then required a 2500-km diameter of the circulation or a large area of deep convection to the south and southeast. After using circulation at $r = 660$ km as a first guess to narrow the choice of grid points, the gyre diameter was "visually determined." As noted in the data and methods section, gyres seem distinct when seen on weather maps and satellites, but the previous definitions of gyres are not objective and thus not reproducible. One goal of this paper was to define a set of objective criteria that satisfy some of the subjective characteristics described first by Lander (1994). The criteria were discussed in the methods section and are given in Table 1. This appendix will provide more details of the process.

Condition 1 in Table 1 insured a large circulation. Condition 2 represents a minimum circulation criterion. Figure A1 shows the radial variation of azimuthally averaged circulation from our three previous studies of gyres. Circulation rose steadily from the center to at least the 1000-km radius. Thereafter it sometimes

continued to increase to a maximum near 1400 km, but most often leveled off and decreased beyond about 1200 km. The minimum 900–1200-km circulation required to identify a gyre (Table 1) was taken as the largest value that was met by all of the times in Figs. A1a–c. The value of $C_{min} = 5.3 \times 10^7\,m^2\,s^{-1}$ is equivalent to a mean tangential wind of $8\,m\,s^{-1}$ over the radial range. Also shown (Fig. A1d) are the circulation for an observed intense tropical cyclone and an ERA-I composite Atlantic category 3–5 tropical cyclone. Both the observed tropical cyclone and the composite ERA-I tropical cyclones revealed circulation approaching zero by $r = 1200$ km. As a result, criterion 2 prevented the vast majority of tropical cyclones from being misidentified as gyres.

Once the existence of a gyre is established, a procedure must be developed to define the center location. Both Chen et al. (2004) and Wu et al. (2013) subjectively defined a center based on 850-hPa wind plots. Molinari and Vollaro (2012) simply used the surface pressure minimum within the gyre. This simple and logical definition failed in the study of Crandall et al. (2014) because a tropical cyclone rotating around the gyre contained the minimum pressure. In their study and in the current study, a circulation criterion was used to define the center (see item 2 below).

The procedure for identifying all gyre times was as follows:

1) Examine every grid point in the 1.5° latitude–longitude ERA-I analyses at 850 hPa, for all June–November days over the 31 years, over the region from 4.5° to 29.5°N and 108°E to 180°. Interpolate the wind components to cylindrical coordinates at each grid point and define circulation and azimuthally averaged tangential velocity in 100-km radial bins out to $r = 2000$ km.
2) Identify every grid point that satisfies the first two conditions in Table 1. This typically produces a cloud of contiguous points at a given time in the region where a gyre is present. Define the gyre center as the grid point with maximum circulation in the 900–1200 km radial range.
3) The gyre track was defined by the sequential locations of center points from step 2 above for every 12 h until the first two conditions in Table 1 were no longer met. If a gyre position jumped by 1000 km or more, it was considered a new gyre. If the lifetime of the gyre did not reach 4 days, it was not included in the analysis.
4) All gyres that satisfied conditions 1–3 in Table 1 were then evaluated for the behavior of tropical cyclones in their vicinity. Any times in which tropical cyclones were present but did not rotate around the gyre center were removed. This eliminated times when the gyre and the tropical cyclone could not be separated.

Figure 6 in the text shows that these criteria produced gyres with a structure similar to that determined by previous subjective methods. In particular, the typical gyre precipitation asymmetry appeared despite it not being a criterion for defining the gyre. This suggests that the objective criteria in Table 1 were successful in isolating disturbances with the classic structure defined by Lander (1994).

REFERENCES

Ashouri, H., K.-L. Hsu, S. Sorooshian, D. K. Braithwaite, K. R. Knapp, L. D. Cecil, B. R. Nelson, and O. P. Prat, 2015: PERSIANN-CDR: Daily precipitation climate data record from multisatellite observations for hydrological and climate studies. *Bull. Amer. Meteor. Soc.*, **96**, 69–83, doi:10.1175/BAMS-D-13-00068.1.

Bi, M., T. Li, M. Peng, and X. Shen, 2015: Interactions between Typhoon Megi (2010) and a low-frequency monsoon gyre. *J. Atmos. Sci.*, **72**, 2682–2702, doi:10.1175/JAS-D-14-0269.1.

Camargo, S. J., and A. H. Sobel, 2005: Western North Pacific tropical cyclone intensity and ENSO. *J. Climate*, **18**, 2996–3006, doi:10.1175/JCLI3457.1.

——, A. W. Robertson, S. J. Gaffney, P. Smyth, and M. Ghil, 2007: Cluster analysis of typhoon tracks: Part II: Large-scale circulation and ENSO. *J. Climate*, **20**, 3654–3676, doi:10.1175/JCLI4203.1.

——, M. C. Wheeler, and A. H. Sobel, 2009: Diagnosis of the MJO modulation of tropical cyclogenesis using an empirical index. *J. Atmos. Sci.*, **66**, 3061–3074, doi:10.1175/2009JAS3101.1.

Carr, L. E., and R. L. Elsberry, 1995: Monsoonal interactions leading to sudden tropical cyclone track changes. *Mon. Wea. Rev.*, **123**, 265–290, doi:10.1175/1520-0493(1995)123<0265:MILTST>2.0.CO;2.

Chan, J. C. L., 1985: Tropical cyclone activity in the northwest Pacific in relation to the El Niño/Southern Oscillation phenomenon. *Mon. Wea. Rev.*, **113**, 599–606, doi:10.1175/1520-0493(1985)113<0599:TCAITN>2.0.CO;2.

Chen, T. C., S.-Y. Wang, M.-C. Yen, and W. A. Gallus Jr., 2004: Role of the monsoon gyre in the interannual variation of tropical cyclone formation over the western North Pacific. *Wea. Forecasting*, **19**, 776–785, doi:10.1175/1520-0434(2004)019<0776:ROTMGI>2.0.CO;2.

Chia, H. H., and C. F. Ropelewski, 2002: The interannual variability in the genesis location of tropical cyclones in the northwest Pacific. *J. Climate*, **15**, 2934–2944, doi:10.1175/1520-0442(2002)015<2934:TIVITG>2.0.CO;2.

Choi, K.-S., C.-C. Wu, and E.-J. Cha, 2010: Change of tropical cyclone activity by Pacific–Japan teleconnection pattern in the western North Pacific. *J. Geophys. Res.*, **115**, D19114, doi:10.1029/2010JD013866.

Corbosiero, K. L., and J. Molinari, 2002: The effects of vertical wind shear on the distribution of convection in tropical cyclones. *Mon. Wea. Rev.*, **130**, 2110–2123, doi:10.1175/1520-0493(2002)130<2110:TEOVWS>2.0.CO;2.

Crandall, B., J. Molinari, and D. Vollaro, 2014: Forecasting challenges associated with tropical cyclones within subtropical gyres. *Wea. Forecasting*, **29**, 99–114, doi:10.1175/WAF-D-13-00053.1.

Dee, D. P., and Coauthors, 2011: The ERA-Interim reanalysis: Configuration and performance of the data assimilation system. *Quart. J. Roy. Meteor. Soc.*, **137**, 553–597, doi:10.1002/qj.828.

Ditchek, S. D., J. Molinari, and D. Vollaro, 2017: Tropical cyclone outflow-layer structure and balanced response to eddy forcing. *J. Atmos. Sci.*, **74**, 133–149, doi:10.1175/JAS-D-16-0117.1.

Frank, W. M., and P. E. Roundy, 2006: The role of tropical waves in tropical cyclogenesis. *Mon. Wea. Rev.*, **134**, 2397–2417, doi:10.1175/MWR3204.1.

Franklin, J. L., S. J. Lord, S. E. Feuer, and F. D. Marks Jr., 1993: The kinematic structure of Hurricane Gloria (1985) determined from nested analyses of dropwindsonde and Doppler radar data. *Mon. Wea. Rev.*, **121**, 2433–2451, doi:10.1175/1520-0493(1993)121<2433:TKSOHG>2.0.CO;2.

Gill, A. E., 1980: Some simple solutions for heat-induced tropical circulation. *Quart. J. Roy. Meteor. Soc.*, **106**, 447–462, doi:10.1002/qj.49710644905.

Holland, G. J., 1995: Scale interaction in the western Pacific monsoon. *Meteor. Atmos. Phys.*, **56**, 57–79, doi:10.1007/BF01022521.

Hurley, J. V., and W. R. Boos, 2015: A global climatology of monsoon low-pressure systems. *Quart. J. Roy. Meteor. Soc.*, **141**, 1049–1064, doi:10.1002/qj.2447.

Kosaka, Y., and H. Nakamura, 2006: Structure and dynamics of the summertime Pacific–Japan teleconnection pattern. *Quart. J. Roy. Meteor. Soc.*, **132**, 2009–2030, doi:10.1256/qj.05.204.

Krishnamurti, T. N., 1971: Tropical east–west circulations during the northern summer. *J. Atmos. Sci.*, **28**, 1342–1347, doi:10.1175/1520-0469(1971)028<1342:TEWCDT>2.0.CO;2.

Lander, M. A., 1994: Description of a monsoon gyre and its effects on the tropical cyclones in the western North Pacific during August 1991. *Wea. Forecasting*, **9**, 640–654, doi:10.1175/1520-0434(1994)009<0640:DOAMGA>2.0.CO;2.

Li, R. C. Y., W. Zhou, and T. Li, 2014: Influences of the Pacific–Japan teleconnection pattern on synoptic-scale variability in the western North Pacific. *J. Climate*, **27**, 140–154, doi:10.1175/JCLI-D-13-00183.1.

Liang, J., and L. Wu, 2015: Sudden track changes of tropical cyclones in monsoon gyres: Full-physics, idealized numerical experiments. *J. Atmos. Sci.*, **72**, 1307–1322, doi:10.1175/JAS-D-13-0393.1.

Liebmann, B., H. H. Hendon, and J. D. Glick, 1994: The relationship between tropical cyclones of the western Pacific and Indian Oceans and the Madden–Julian oscillation. *J. Meteor. Soc. Japan*, **72**, 401–411.

Molinari, J., and D. Vollaro, 2012: A subtropical cyclonic gyre associated with interactions of the MJO and the midlatitude jet. *Mon. Wea. Rev.*, **140**, 343–357, doi:10.1175/MWR-D-11-00049.1.

——, and ——, 2013: What percentage of western North Pacific tropical cyclones form within the monsoon trough? *Mon. Wea. Rev.*, **141**, 499–505, doi:10.1175/MWR-D-12-00165.1.

——, K. Lombardo, and D. Vollaro, 2007: Tropical cyclogenesis within an equatorial Rossby wave packet. *J. Atmos. Sci.*, **64**, 1301–1317, doi:10.1175/JAS3902.1.

Nakazawa, T., 1988: Tropical super clusters within intraseasonal variations over the western Pacific. *J. Meteor. Soc. Japan*, **66**, 823–839.

Nitta, T., 1987: Convective activities in the tropical western Pacific and their impact on the Northern Hemisphere summer circulation. *J. Meteor. Soc. Japan*, **65**, 373–390.

Ritchie, E. A., and G. J. Holland, 1999: Large-scale patterns associated with tropical cyclogenesis in the western Pacific. *Mon. Wea. Rev.*, **127**, 2027–2043, doi:10.1175/1520-0493(1999)127<2027:LSPAWT>2.0.CO;2.

Sobel, A. H., and C. S. Bretherton, 1999: Development of synoptic-scale disturbances over the summertime tropical northwest Pacific. *J. Atmos. Sci.*, **56**, 3106–3127, doi:10.1175/1520-0469(1999)056<3106:DOSSDO>2.0.CO;2.

Tsuyuki, T., and K. Kurihara, 1989: Impact of convective activity in the western tropical Pacific on the East Asian summer circulation. *J. Meteor. Soc. Japan*, **67**, 231–247.

Wakabayashi, S., and R. Kawamura, 2004: Extraction of major teleconnection patterns possibly associated with the anomalous summer climate in Japan. *J. Meteor. Soc. Japan*, **82**, 1577–1588, doi:10.2151/jmsj.82.1577.

Wheeler, M. C., and H. H. Hendon, 2004: An all-season real-time multivariate MJO index: Development of an index for monitoring and prediction. *Mon. Wea. Rev.*, **132**, 1917–1932, doi:10.1175/1520-0493(2004)132<1917:AARMMI>2.0.CO;2.

Wu, L., H. Zong, and J. Liang, 2011: Observational analysis of sudden tropical cyclone track changes in the vicinity of the East China Sea. *J. Atmos. Sci.*, **68**, 3012–3031, doi:10.1175/2010JAS3559.1.

——, ——, ——, 2013: Observational analysis of tropical cyclone formation associated with monsoon gyres. *J. Atmos. Sci.*, **70**, 1023–1034, doi:10.1175/JAS-D-12-0117.1.